remote sensing

MDPI

Article

Integrated Analysis of Water Ice Detection in Erlanger Crater, Lunar North Pole: Insights from Chandrayaan-1 Mini-SAR and Chandrayaan-2 DFSAR Data

Chandani Sahu [1,*], Shashi Kumar [2], Himanshu Govil [1] and Shovan Lal Chattoraj [3]

[1] Department of Applied Geology, National Institute of Technology, Raipur 492010, Chhattisgarh, India; hgovil.geo@nitrr.ac.in
[2] Photogrammetry & Remote Sensing Department, Indian Institute of Remote Sensing, Indian Space Research Organisation, Dehradun 248001, Uttarakhand, India; shashi@iirs.gov.in
[3] Geosciences Department, Indian Institute of Remote Sensing, Indian Space Research Organisation, Dehradun 248001, Uttarakhand, India; shovan@iirs.gov.in
* Correspondence: chandanisahu25@gmail.com

Abstract: The characterization of the lunar surface and subsurface through the utilization of synthetic aperture radar data has assumed a pivotal role in the domain of lunar exploration science. This investigation concentrated on the polarimetric analysis aimed at identifying water ice within a specific crater, designated Erlanger, located at the lunar north pole, which is fundamentally a region that is perpetually shaded from solar illumination. The area that is perpetually shaded on the moon is defined as that region that is never exposed to sunlight due to the moon's slightly tilted rotational axis. These permanently shaded regions serve as cold traps for water molecules. To ascertain the presence of water ice within the designated study area, we conducted an analysis of two datasets from the Chandrayaan mission: Mini-SAR data from Chandrayaan-1 and Dual-Frequency Synthetic Aperture Radar (DFSAR) data from Chandrayaan-2. The polarimetric analysis of the Erlanger Crater, located in a permanently shadowed region of the lunar north pole, utilizes data from the Dual-Frequency Synthetic Aperture Radar (DFSAR) and the Mini-SAR. This study focuses exclusively on the L-band DFSAR data due to the unavailability of S-band data for the Erlanger Crater. The crater, identified by the PSR ID NP_869610_0287570, is of particular interest for its potential water ice deposits. The analysis employs three decomposition models—m-delta, m-chi, and m-alpha—derived from the Mini-SAR data, along with the H-A-Alpha model known as an Eigenvector and Eigenvalue model, applied to the DFSAR data. The H-A-Alpha helps in assessing the entropy and anisotropy of the lunar surface. The results reveal a correlation between the hybrid polarimetric models (m-delta, m-chi, and m-alpha) and fully polarimetric parameters (entropy, anisotropy, and alpha), suggesting that volume scattering predominates inside the crater walls, while surface and double bounce scattering are more prevalent in the right side of the crater wall and surrounding areas. Additionally, the analysis of the circular polarization ratio (CPR) from both datasets suggests the presence of water ice within and around the crater, as values greater than 1 were observed. This finding aligns with other studies indicating that the high CPR values are indicative of ice deposits in the lunar polar regions. The polarimetric analysis of the Erlanger Crater contributes to the understanding of lunar polar regions and highlights the potential for future exploration and resource utilization on the Moon.

Keywords: Chandrayaan-1 Mini-SAR; Chandrayaan-2 DFSAR; permanently shadowed regions; polarimetry; circular polarization ratio

check for updates

Academic Editor: Cyril Grima

Received: 15 October 2024
Revised: 4 December 2024
Accepted: 14 December 2024
Published: 26 December 2024

Citation: Sahu, C.; Kumar, S.; Govil, H.; Chattoraj, S.L. Integrated Analysis of Water Ice Detection in Erlanger Crater, Lunar North Pole: Insights from Chandrayaan-1 Mini-SAR and Chandrayaan-2 DFSAR Data. *Remote Sens.* **2025**, *17*, 31. https://doi.org/10.3390/rs17010031

Copyright: © 2024 by the authors. Licensee MDPI, Basel, Switzerland. This article is an open access article distributed under the terms and conditions of the Creative Commons Attribution (CC BY) license (https://creativecommons.org/licenses/by/4.0/).

1. Introduction

The Moon, Earth's only natural satellite, is located approximately 384,400 km away and is the closest celestial body to our planet [1]. It is the only extraterrestrial body that humans have visited and explored [2]. Understanding the formation and evolution of planetary bodies, including the Moon, is crucial for studying their current geological states [3].

Lunar exploration has provided valuable insights into various aspects such as lunar geology, the Moon's origin, the evolution of its crust and mantle, surface composition, impact cratering processes, space weathering, and potential resources for human use [4,5]. Historically, several theories about the Moon's formation existed, including the idea that it was a hollow, dry wasteland or a fluffy rock body [6]. However, these theories were largely dispelled following the Apollo missions, which revealed that the Moon's surface is characterized by numerous craters formed by impacts from meteorites and comets. Additionally, the Apollo mission yielded substantial evidence indicating the existence of an atmospheric layer on the lunar surface [7]. It has been determined that the moon's atmosphere comprises atypical gases such as potassium and sodium, along with trace quantities of water molecules, carbon dioxide, argon, methane, and ammonia, as well as neon, helium, and hydrogen atoms [8]. Studies have also been carried out to elaborate the petrophysical [9], geomorphological [10–12], and mineralogical [13,14] properties of the lunar surface.

In addition to the Apollo mission, numerous other missions, including SELENE (Kaguya) from the Japan Aerospace Exploration Agency, and the Chang'e series from the China National Space Administration, as well as the Lunar Reconnaissance Orbiter from the United States, were initiated, resulting in the acquisition of substantial information regarding the lunar surface environment and atmosphere, and contributing significantly to the understanding of the historical evolution of the Moon. A study published in Nature Geoscience reveals a critical reaction that occurred deep within the Moon approximately 3.5 billion years ago that affected the magma composition and distribution across its surface [15]. Among such missions are India's Chandrayaan-1 and Chandrayaan-2, which were launched on 22 October 2008 and 22 July 2019, respectively, and which investigated the lunar surface environment, yielding crucial insights regarding the Moon [16,17]. Mini-SAR and DFSAR represent the synthetic aperture radar sensors integrated into these two missions, which facilitate the physical characterization of the lunar surface environment [2,10,18,19] as well as the identification of entrapped water ice particles within the lunar regolith. Synthetic aperture radar (SAR) data are predominantly influenced by a range of system parameters, which encompass the wavelength, the angle of incidence, and polarization, as well as different target parameters that involve the electrical and structural characteristics of the object under observation [20]. The majority of the lunar pole comes under the permanently shadowed regions that never receive sunlight. By analyzing these PSRs with synthetic aperture radar data, one can gain valuable insights about the region and aid in the physical characterization of the lunar surface environment, which is important for researching water ice [21]. Recent studies have emphasized how the roughness properties of lunar craters can indicate crater degradation and provide insight into their ages [22]. Furthermore, research has shown that elevated circular polarization ratios (CPRs) combined with significant volume scattering are indicative of ice deposits in these regions [23].

In the past, a number of studies have been carried out to use SAR data for the physical characterization and polarimetric analysis of the lunar surface environment in order to look into the possibility of water ice [24]. This study's primary goal is to discover water ice in the Erlanger Crater by utilizing the S band of hybrid polarimetry Mini-SAR data

from Chandrayaan-1 and the L band of fully polarimetry DFSAR data from Chandrayaan-2. Our investigation is concentrated on this crater due to its potential classification as icy or its categorization under regolith situated atop ice [25]. Ref. [26] also conducted an investigation into the presence of water ice within the Erlanger Crater utilizing the bistatic angle and CPR methodology. Due to the fact that the crater is located in an entirely dark environment and numerous prior investigations have been undertaken regarding this crater, it thus serves as a pertinent area of study for our research.

2. Study Area

The area chosen for investigation in this research endeavor is the Erlanger Crater, located within the lunar north polar region. This particular crater is situated in proximity to the Peary and Byrd craters. A substantial portion of this crater resides within a region that is perpetually shrouded in darkness, thereby suggesting an increased possibility of the presence of water ice within these craters. Erlanger Crater holds considerable importance in the quest for lunar water resources. The regions within the crater that are perpetually shrouded in darkness, referred to as permanently shadowed regions (PSRs), are hypothesized to contain deposits of water ice, which may be the remnants of impacts from comets. The crater is positioned at the geographical coordinates of 86.94°N and 28.62°E, having a diameter of approximately 9.9 km [25]. The area covered by the crater is 90 km^2 [26]. Ref. [27] conducted an investigation into the water ice signature derived from the Chandrayaan-1 M^3 dataset, ultimately determining that roughly 3.8% of the identified cold traps display ice exposures, one of which includes the Erlanger Crater region. The crater is assumed to have a flat basal plain with a slope of approximately 1.7 degrees and lacks a central peak [26]. The basal surface of the Erlanger Crater is perpetually shrouded in darkness, thereby inhibiting any ice that may have accumulated from undergoing sublimation into vapor [28]. This situation is in stark contrast to numerous other lunar craters that receive solar illumination on their floors during particular intervals of the lunar day, where any ice that exists would be dissipated into outer space. The crater rim rises 200 m above the surrounding area, formed by the deposition of impact ejecta, and is characterized by the absence of rays and wall terracing [26].

3. Materials and Methods

The datasets used for the study area are from the Chandrayaan-1 and Chandrayaan-2 missions, which are Mini-SAR data and DFSAR data. Chandrayaan-1 represents India's inaugural lunar exploration mission, which was initiated in October 2008 and included a variety of scientific payloads, among which the Mini-SAR sensor is notable. The primary objective of the Mini-SAR sensor was to investigate the possibility of water ice particles in the permanently shaded areas of the lunar polar regions [29]. The Mini Synthetic Aperture Radar (SAR) sensor operates S band of microwave range, particularly targeting the northern polar region, with coverage between 79.06°N and 87.65°N latitude and longitudes from 342.23°W to 70.66°E. The data, obtained during orbit 1665 of the nominal mission phase, have an incidence angle of 34.59° and a wavelength range of 12.6 cm. Each strip of data acquired from the Mini-SAR exhibits a spatial resolution of 75 m, encompassing a swath width of 8 km. The Mini-SAR strip utilized in this study is fsb_01665_1cd_xiu_84n056_v1, a Level 1 calibrated dataset. The azimuth and range resolutions of the dataset are 163.55 m and 162.13 m, respectively, with scaled pixel dimensions of 75 m × 75 m. The data consist of four bands: horizontal receive intensity, vertical receive intensity, cross-power intensity (real), and cross-power intensity (imaginary). The primary conclusion drawn from the Mini-SAR data was that the north pole of the Moon's circular polarization ratio showed values in the range of 0.1 to 0.3. Additionally, certain craters were identified that

displayed higher CPR values, between 0.6 and 1.7, in their interiors, while lower CPR values, ranging from 0.2 to 0.4, were observed around the exterior and near the rims of these craters [2]. Chandrayaan-2, the second lunar mission to the moon, was successfully launched in July 2019 [24]. One of the key instruments onboard was the Dual-Frequency Synthetic Aperture Radar (DFSAR), a microwave radar that operated at both S-band (12 cm wavelength) and L-band (24 cm wavelength) frequencies. DFSAR was developed to examine the lunar surface and subsurface from a height of around 100 km around the moon. The Dual-Frequency Synthetic Aperture Radar (DFSAR) carried by Chandrayaan-2 is a groundbreaking instrument for lunar exploration. It is the first L-band SAR to study the lunar surface, with the ability to penetrate deep into the lunar subsurface. DFSAR also offers important insights into the physical characteristics of the lunar regolith as it is the first fully polarimetric SAR orbiting the moon. The DFSAR instrument on Chandrayaan-2 is capable of operating in single, dual, and hybrid circular polarimetry modes to acquire high-resolution images of the lunar surface. These images have a spatial resolution of 75 m and were captured at incidence angles ranging from 9.6° to 36.9°, allowing for detailed analysis of the lunar terrain [30]. The DFSAR data strip employed in this investigation is ch2_sar_ncxl_20201004t232400993_d_fp_d18, which pertains to L-band data functioning at an incidence angle of 25.99°. The data were collected during orbit number 4963 on 4 October 2020, with a start time of 23:24:00.993 UTC and a stop time of 23:25:46.973 UTC. The SAR operated in StripMap mode with a nominal swath of 10 km, capturing data in various polarimetric configurations, including HH, HV, VH, and VV, stored as slant-range complex images in GeoTIFF format. The antenna footprint ranged from 22.5 to 34 km for L band and 11.2 to 16.8 km for S band over a range coverage region from 16 km to 70 km off-nadir. The data resolution was high, with input resolutions of 21.62 m along-track and 19.99 m across-track, processed into a pixel spacing of 9.59 m. Table 1 provides the details of Mini-SAR and DFSAR data used in the present study.

Table 1. Datasets used in the present study.

S.No.	Sensor/Satellite Name	Strip Id	Band
1	Mini-SAR/Chandrayaan-1	fsb_01665_1cd_xiu_84n056_v1	S
2	DFSAR/Chandrayaan-2	ch2_sar_ncxl_20201004t232400993_d_fp_d18	L

As illustrated in Figure 1, the Erlanger Crater is situated within the region of permanent shadow in the lunar north pole, designated with the PSR id NP_869610_0287570. The image strip presented in Figure 1 depicts a DFSAR L-band composite image that nearly encompasses the entirety of the Erlanger Crater.

The methodology followed in this study is illustrated in Figure 2. The Mini-SAR dataset represents a hybrid polarimetric dataset that was acquired in Synthetic Aperture Radar (SAR) mode. The Mini-SAR dataset utilized in this research constitutes a Level 1 calibrated product, which has undergone radiometric and polarimetric calibration processes. Each data product encompasses four channels of raw data, $|LH|^2$, $|LV|^2$, real part LH*LV, and imaginary part LH*LV, all of which are provided without any further processing [31]. The Stokes vector S is formed primarily by these four channels. The Stokes parameters elucidate the polarization characteristics of electromagnetic radiation and are articulated as follows: $S1$ indicates the cumulative intensity of the electromagnetic signal, $S2$ represents difference between the horizontal and vertical components, and $S3$ and $S4$ represent the real and imaginary parts that correspond to the cosine and sine of the mean phase difference between the horizontally and vertically polarized elements of the electromagnetic field [6]. The datasets are procured from the Planetary Data System (PDS) Geosciences node and are

formatted as images. Using the PDS data, the Stokes parameters were derived from these four channels or bands by applying Stokes equations, which can be represented as follows:

$$\begin{pmatrix} S1 \\ S2 \\ S3 \\ S4 \end{pmatrix} = \begin{pmatrix} band\ 1 + band\ 2 \\ band\ 1 - band\ 2 \\ 2\ X\ band\ 3 \\ -2\ X\ band\ 4 \end{pmatrix} = \begin{pmatrix} < |E_H|^2 + |E_V|^2 > \\ < |E_H|^2 - |E_V|^2 > \\ 2Re < E_H E_V{}^* > \\ -2Im < E_H E_V{}^* > \end{pmatrix} \quad (1)$$

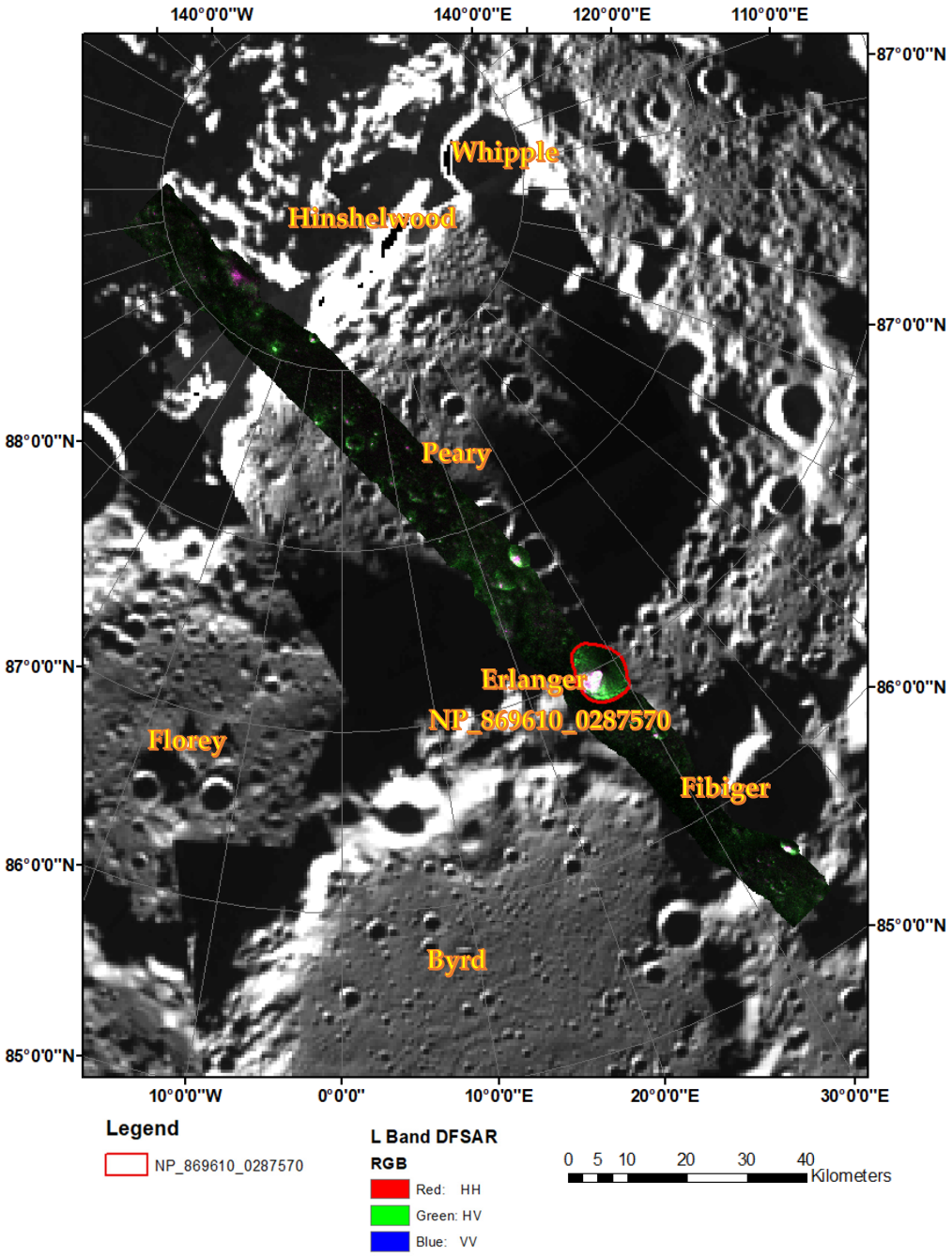

Figure 1. L-band color composite DFSAR for the north pole of the lunar surface with the PSR id of Erlanger. Clementine image is used as base map to show the north pole of lunar surface.

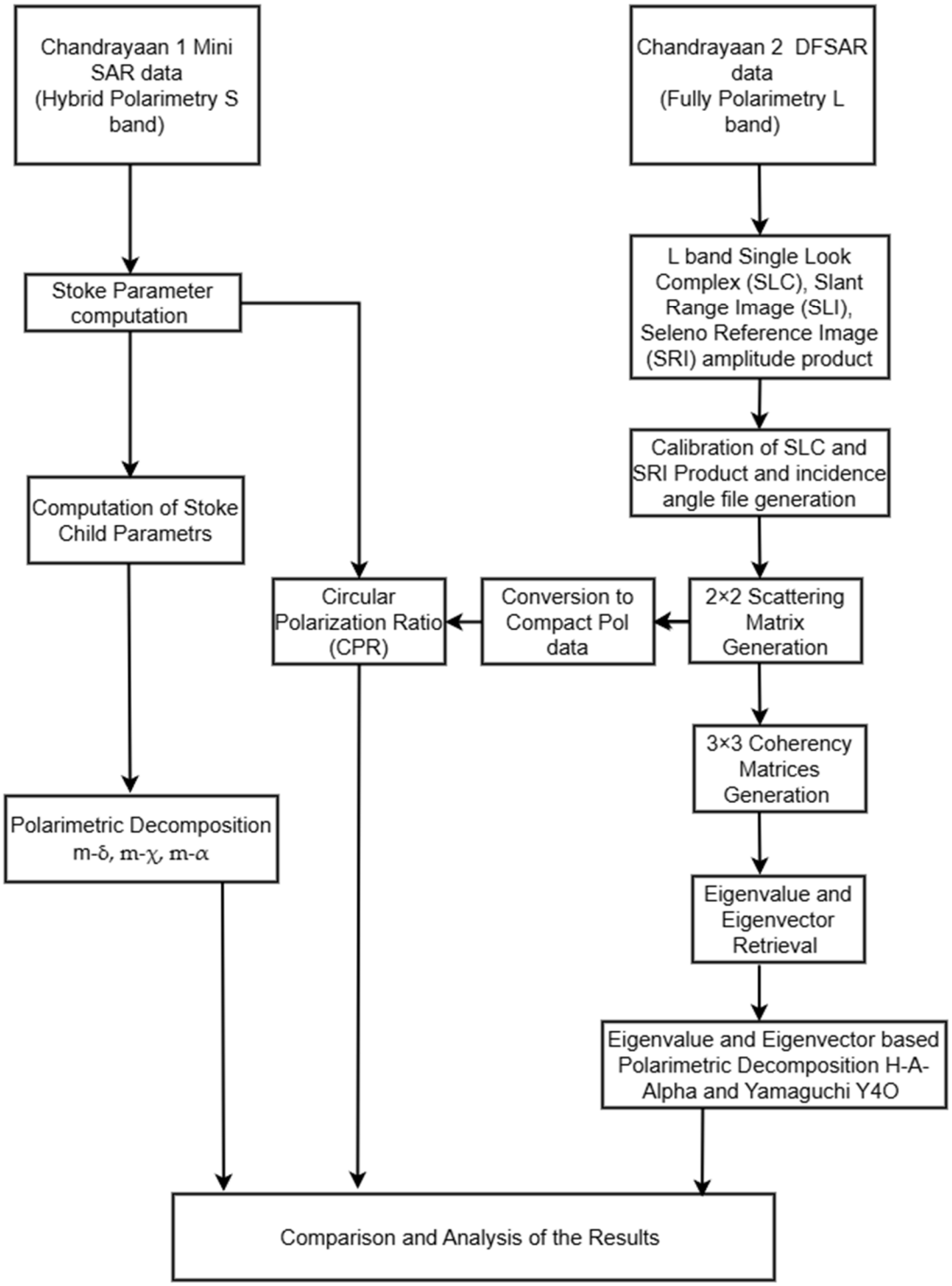

Figure 2. Detailed methodology flow diagram.

Here, the Stokes vectors are denoted by $S1$, $S2$, $S3$, and $S4$, while the horizontal and vertical components of the electromagnetic field's polarization are represented by E_H and E_V, respectively. The complex conjugate associated with the horizontal or vertical polarization components is indicated by the symbol '*' [6]. The overall intensity of the backscattered field is represented by the first Stokes parameter, $S1$, and the difference between the horizontal and vertical components of polarization is represented by the second Stokes parameter, $S2$. Moreover, the real and imaginary components are denoted by the third and fourth Stokes parameters, $S3$ and $S4$, respectively.

Following the calculation of Stokes parameters, Stokes child parameters were computed, including polarization angle (α), relative phase difference (δ), ellipticity angle (χ), and degree of polarization (m). These child parameters are further used in generating decomposition models. The following equations are used to calculate the child parameters:

$$m = \sqrt{S2^2 + S3^2 + S4^2}/S1 \tag{2}$$

$$\delta = tan^{-1} S4/S3 \tag{3}$$

$$\chi = 1/2 sin^{-1}(-S4/m * S1) \tag{4}$$

$$\alpha = 1/2 tan^{-1} \frac{\sqrt{S2^2 + S3^2}}{S4} \tag{5}$$

In these above Equations $S1$, $S2$, $S3$, and $S4$ are Stokes parameters. The degree of polarization m is an indicator of polarized and diffused scattering and the value varies between 1 to 0, where 1 indicates a completely polarized wave and 0 indicates significant diffused scattering, which may occur in rough terrains or heterogeneous materials. m is calculated by Equation (2). Relative phase difference δ is indicative of double bounce scattering and is calculated as per Equation (3). Ellipticity angle χ, also called the phase parameter, is sensitive to dihedral scattering and calculated by using Equation (4).

The physical characteristics of the lunar surface and the water ice contained within the lunar regolith are influenced by pivotal parameters such as CPR, Entropy, and Anisotropy, as well as other child parameters calculated in the present work. An elevated value of CPR > 1 signifies increased surface roughness and volumetric scattering, which facilitates the identification of water ice sequestered within crater regions, as evidenced by decomposition models m-δ, m-χ, and m-α, along with H-A-Alpha, and Yamaguchi. Through the integration of these polarimetric parameters and decomposition methodologies utilizing Mini-SAR and DFSAR datasets, the approach permits a more refined interpretation of Mini-SAR data and DFSAR data, establishing a direct association between polarization characteristics and the tangible presence of water ice, as well as the heterogeneity of regolith in lunar permanently shadowed regions.

3.1. m-δ Decomposition

The m-δ decomposition technique was developed and proposed by Raney [32]. The m-δ decomposition methodology is extensively employed within both marine and terrestrial research domains to distinguish between double bounce and surface bounce scattering, where 'm' signifies the polarity characteristics of backscatter and double bounce scattering is indicated by δ. The state of polarization of an electromagnetic wave is characterized by the degree of polarization and the relative phase difference, both of which are obtained from the Stokes parameters as given in Equations (2) and (3). The parameter m is situated within the interval of 0 to 1, wherein the value 0 represents depolarized backscatter, while the value 1 indicates polarized backscatter, while the variable delta is confined within the range of -180° to 180°, where -180° signifies that the rotational direction is right circular and 180° indicates that the rotational direction is left circular. The m-δ decomposition equations for surface scattering, double bounce scattering, and volumetric scattering are given below:

$$s = \sqrt{m * S1 * \frac{(1 + sin\delta\ )}{2}} \tag{6}$$

$$d = \sqrt{m * S1 * \frac{(1 - sin\delta)}{2}} \tag{7}$$

$$v = \sqrt{S1 * (1 - m)} \tag{8}$$

where s, d, and v represent surface, double bounce, and volumetric scattering respectively.

3.2. m-χ Decomposition

The m-χ decomposition methodology was articulated and introduced by [32], who employed this analytical approach within the context of hybrid polarimetric data. This particular decomposition method is predominantly utilized for the purpose of distinguishing surface scattering phenomena from double bounce scattering occurrences. Stokes parameters are used to determine the degree of polarization (m) and the ellipticity angle (χ), which, together, make up the m-χ decomposition. The range of values for χ fluctuates between -45° and 45°, a variation that is dependent upon the specific scattering mechanisms involved. The equation of surface, double bounce, and volumetric scattering for the m-χ decomposition technique is given by the following equations:

$$s = \sqrt{m * S1 * \frac{(1 - sin2\chi)}{2}} \tag{9}$$

$$d = \sqrt{m * S1 * \frac{(1 + sin2\chi)}{2}} \tag{10}$$

$$v = \sqrt{S1 * (1 - m)} \tag{11}$$

where s, d, and v represent surface, double bounce, and volumetric scattering, respectively.

3.3. m-α Decomposition

The m-alpha decomposition methodology is based on Eigenvector analysis of hybrid polarimetric data and is closely related to the H/alpha decomposition approach used for hybrid polarimetric datasets [33,34]. The m-alpha technique analyzes the degree of polarization (m) and polarization angle (alpha), while the H/alpha decomposition extracts information on Entropy (H) and alpha angle using the coherency matrix [35,36]. The α parameter can be computed by utilizing the Stokes vector as given in Equation (5) [37]. In the present investigation, the subsequent equation is employed to compute the alpha angle as delineated in the following [38]:

$$\alpha = \frac{1}{2} tan^{-1}\left(\frac{\sqrt{S2^2 + S3^2}}{\pm S4}\right) \tag{12}$$

Using Equations (2) and (12), the surface, double bounce, and volumetric scattering for m-α technique can be calculated by following equations [2]:

$$s = \sqrt{m * S1 * \frac{(1 + cos2\alpha)}{2}} \tag{13}$$

$$d = \sqrt{m * S1 * \frac{(1 - cos2\alpha)}{2}} \tag{14}$$

$$v = \sqrt{S1 * (1 - m)} \tag{15}$$

where s, d, and v represent surface, double bounce, and volumetric scattering, respectively. The scattering angle, or α, ranges from 0 to 90°. A value of 0 denotes surface scattering, a value of 45° suggests volumetric scattering, and a value of 90° denotes double bounce scattering. The Stokes parameters are also used for the calculation of circular polarization ratio (CPR), which can be used to find the water ice in the crater [39]. The ability to

detect water ice on the lunar surface is largely dependent on CPR. It is defined as the ratio of transmitted power in the opposite sense to the ratio of received power in the same meaning [40,41]. The following equation can be used to calculate the CPR:

$$CPR = \frac{SC}{OC} = \frac{S1 - S4}{S1 + S4} \tag{16}$$

where SC is received power in the same sense and OC is the transmitted power in the opposite sense. It is derived using Stokes parameters $S1$ and $S4$, where $S1$ represents the difference between the horizontal and vertical linear polarization components and $S4$ represents the difference between right-handed and left-handed circular polarization components as mentioned in Equation (16). A CPR value greater than one denotes a rough surface, while a value less than one suggests surface scattering.

In conjunction with the circular polarization ratio, the angle of incidence also exerts a significant influence on radar backscattering phenomena. [42] investigated the effect of incidence angle on radar scattering from icy lunar surfaces at 13 cm and 4 cm wavelengths. For radar studies of the Moon and Mars, the mean radar cross-section is explained as a combination of specular and diffuse elements. The specular component arises from mirror-like reflections off large surfaces (10 or more radar wavelengths in size) that are flat to within one-tenth of the radar wavelength and aligned perpendicularly to the radar beam. Since the lunar surface features gentle undulations with root mean square (rms) slopes of approximately 2°–4° in the maria and 6°–8° in the terra, the specular scattering from the surface–regolith boundary primarily contributes to opposite-sense circular (OC) echoes, which diminish rapidly as the incidence angle increases. Beyond an incidence angle of about 35°, the strength of these OC echoes follows a $\cos^{1.5}(\theta)$ relationship. Additionally, subsurface layers within crater ejecta, as inferred from Apollo core tube data, could produce average OC cross-sections with a similar $\cos^{1.5}(\theta)$ dependence. Meanwhile, the diffuse scattering component is linked to rocks of sizes ranging from one-tenth to 10 radar wavelengths, located either on the surface or within the radar's penetration depth—up to 10 wavelengths in the maria and as much as 40 wavelengths in the terra. The same-sense circular (SC) polarization at centimeter wavelengths exhibits a $\cos(\theta)$ dependence across all incidence angles.

3.4. Decomposition Modelling for DFSAR Data

Two different types of decomposition techniques—H-A-Alpha and Yamaguchi four-component decomposition—were employed in the present work to characterize the Erlanger Crater using the L-band DFSAR dataset. These two-decomposition techniques were used in this study to evaluate and compare the findings acquired from the Mini-SAR S-band decomposition techniques, specifically m-α, m-χ, and m-δ.

The Eigenvalue–Eigenvector decomposition is the foundation of the H-A-Alpha decomposition and it is also known as the Cloude–Pottier decomposition [43]. Entropy (H) is a measure of the degree of randomness in a system. The value of Entropy (H) varies between 0 and 1, where H = 0 indicates surface scattering and H = 1 indicates volumetric scattering. In other words, a low entropy value (closer to 0) suggests that the scattering is dominated by surface features, while a high entropy value (closer to 1) indicates that the scattering is more influenced by volumetric or internal structures. Alpha (α) is a polarization angle that lies between 0° and 90°. The value of Alpha 0° indicates surface scattering, where the scattering is primarily caused by interactions with the surface of an object or medium. When $\alpha = 45°$, it indicates volumetric scattering, which occurs when the scattering is influenced by the internal structure or volume of the object or medium. Finally, a value of $\alpha = 90°$ indicates double bounce scattering, which occurs when the signal bounces off

two surfaces before returning to the sensor. A parameter called Anisotropy (A) denotes non-similarity and is used to supplement entropy [44].

The Yamaguchi four-component decomposition methodology encompasses four distinct components, specifically surface scattering, volumetric scattering, double bounce scattering, and helix scattering, with the latter component being constituted by either left-handed or right-handed helix scattering [43].

4. Results and Discussion

4.1. Characterization of Erlanger Crater

Erlanger Crater, located at the lunar north pole, is a permanently shadowed region that has been studied using various polarimetric decomposition techniques. The characterization of the crater was performed using S-band hybrid polarimetry Mini-SAR data, which included the m-delta (δ), m-chi (χ), and m-alpha (α) decompositions, along with the circular polarization ratio. The parameters m, δ, χ, and α were computed utilizing Stokes vectors for the purpose of generating various decomposition techniques. These distinct decomposition models facilitate the characterization of both surface and subsurface attributes within the designated study area. The results derived from these diverse decomposition methodologies yield three distinct types of scattering phenomena originating from the surface, specifically surface scattering, double bounce scattering, and volumetric scattering. The three scattering mechanisms are depicted in RGB imagery, which will aid in the analysis of the morphological characteristics of the crater, as well as yield significant findings, such as the water ice's existence within this permanently shaded crater. Additionally, the Yamaguchi four-component decomposition technique, the H-A-Alpha decomposition, and the CPR were calculated using the L band of fully polarimetric DFSAR data in order to investigate the various scattering mechanisms within the study area.

4.2. (m-δ) Decomposition

The m-delta decomposition methodologies encompass two parameters, m and delta, the results of which were analyzed through three distinct scattering mechanisms, specifically surface, volumetric scattering, and double bounce scattering, as illustrated in Figure 3a,b and Figure 4a, respectively. The RGB composite depicting these three different scattering types is presented in Figure 4b, which represents the scattering pattern as well as the ejecta emanating from the crater. In the RGB image, the blue color signifies surface scattering, the red denotes double bounce scattering, and the green color represents volumetric scattering.

As shown in Figures 3 and 4, the corners of the crater exhibit brighter surfaces, indicating the presence of surface and double bounce scattering in most regions. In cotrast, volumetric scattering is predominantly observed within the craters. Along the crater's steep sides, where the incident wave reflects back to the sensor directly, surface scattering takes place. Due to the dihedral nature of the lunar surface and the crater walls, double bounce scattering is observed near the crater's margins and in the vicinity. Volumetric scattering intensifies from the crater walls toward the interior, likely due to either a rough surface or the presence of ice, which contributes to the diffused scattering. The value of surface scattering is between 0.05 to 0.4, double bounce is in the range of 0.05 to 0.5, whereas the volumetric scattering value is between 0.05 to 0.5, which is higher than surface scattering.

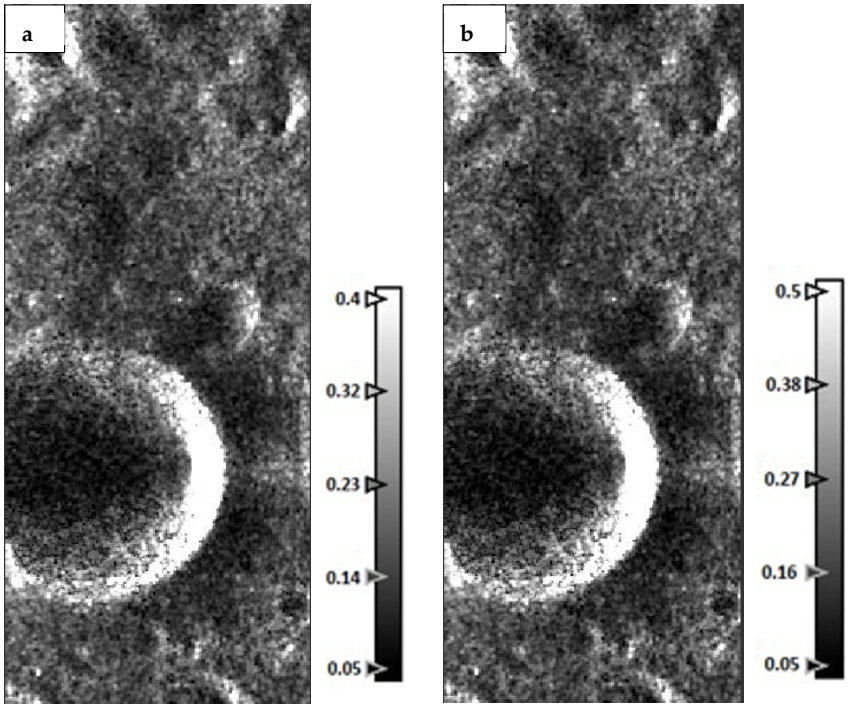

Figure 3. m-delta (δ) decomposition of Mini-SAR data Chandrayaan-1: (**a**) surface scattering; and (**b**) double bounce scattering.

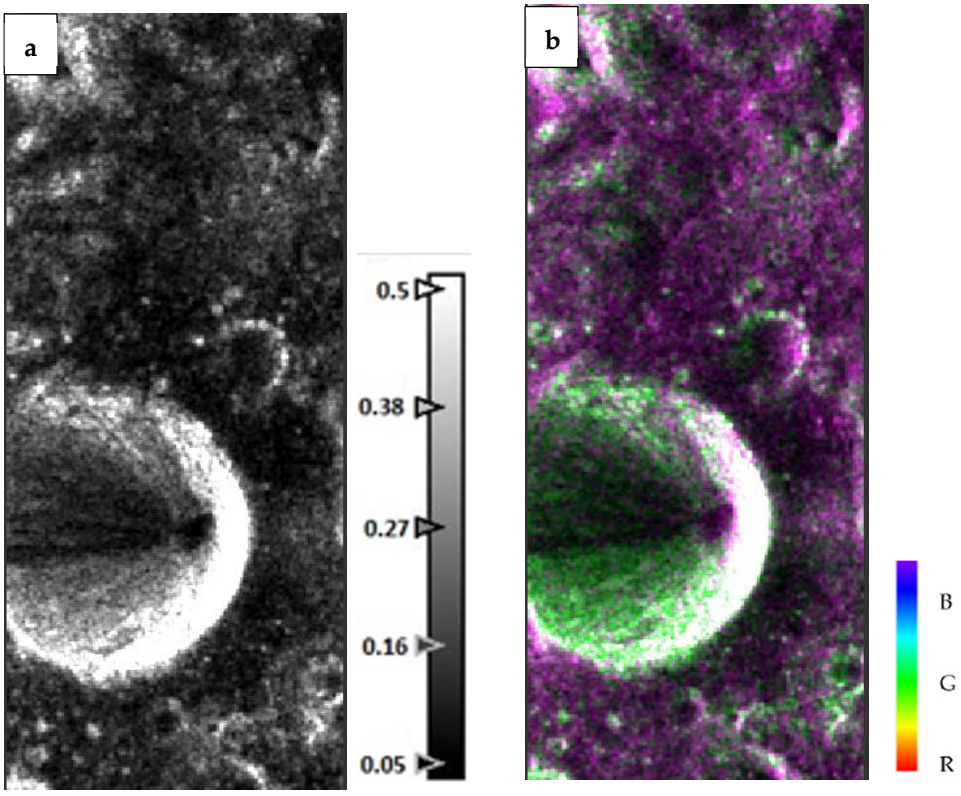

Figure 4. m-delta (δ) decomposition of Mini-SAR data Chandrayaan-1: (**a**) volumetric Scattering; and (**b**) RGB composite image, where G stands for volumetric, R for double bounce, and B for surface scattering.

4.3. m-chi (m-χ) Decomposition

The results from the m-chi decomposition for the study area utilizing Mini-SAR data are illustrated in Figures 5 and 6, where Figure 6b is presented as an RGB color image. Figure 5a,b and Figure 6a represent three types of scattering—surface scattering, double bounce scattering, and volume scattering, respectively—depicted in grayscale images. Compared to m-delta images, the m-chi images yield superior results. Double bounce scattering is distinctly visible in the RGB composite images along the crater walls and the lunar surface. Surface scattering is evident on the steep walls of the crater, while volumetric scattering is observed along the crater walls moving toward the center. In this RGB image, all three scattering mechanisms are easily distinguishable.

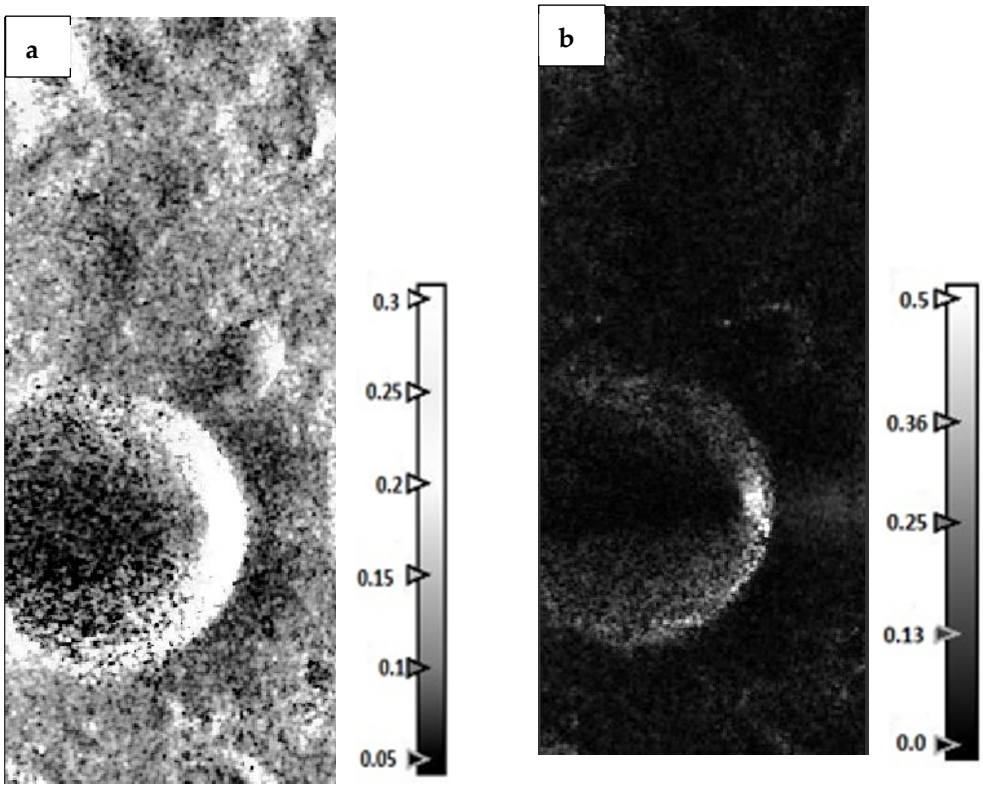

Figure 5. m-chi (χ) decomposition of Mini-SAR data Chandrayaan-1: (**a**) surface Scattering; and (**b**) double bounce scattering.

In the RGB composite image derived from the m-chi decomposition technique as shown in Figure 1b, high volumetric scattering occurs inside the crater as seen in the m-delta decomposition model. The prominence of volumetric scattering suggests that the interior of the crater may have a rough surface or possibly contain water ice, which contributes to the diffused scattering in that area. The red color in the figure indicates the presence of double bounce scattering occurring along the crater walls, where electromagnetic waves reflect off the surface and then bounce back from the wall before reaching the sensor. In the lower right corner of the crater, a small amount of surface scattering is represented in blue, indicating that this area has a sufficiently smooth surface to reflect light effectively.

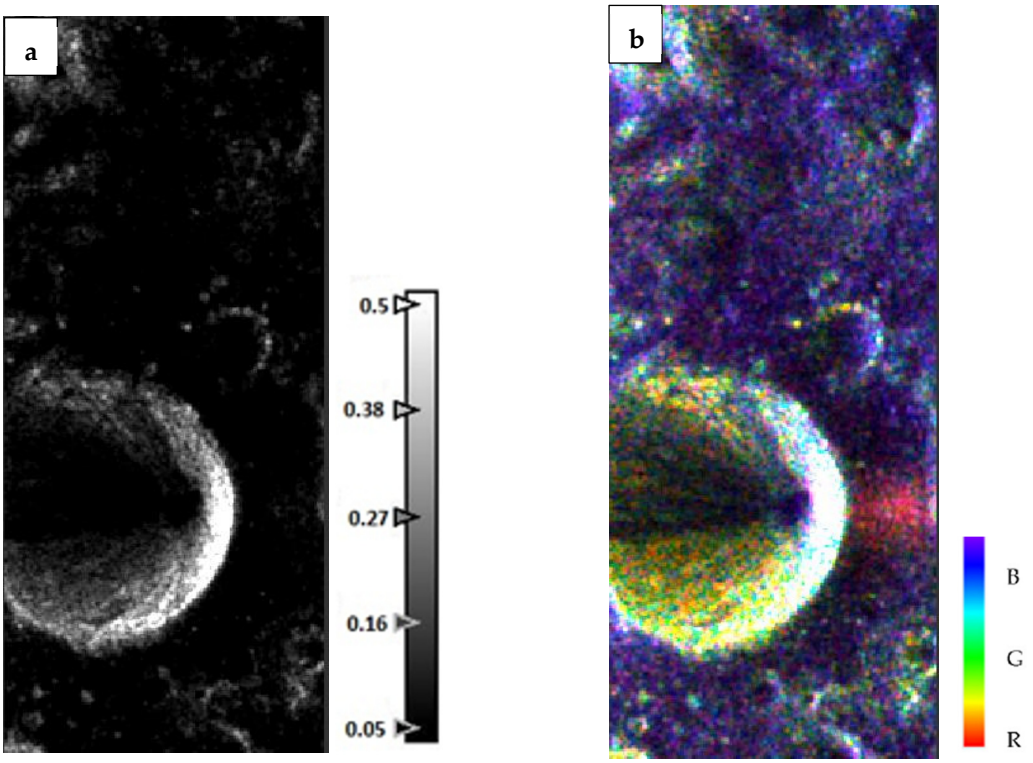

Figure 6. m-chi (χ) decomposition of Mini-SAR data Chandrayaan-1: (**a**) volumetric Scattering; and (**b**) RGB composite image, where G stands for volumetric, R for double bounce, and B for surface scattering.

4.4. m-Alpha (m-α) Decomposition

Figures 7 and 8 show the results obtained from the m-alpha decomposition technique for the Erlanger Crater as seen by Mini-SAR data. Figures 7a,b and 8a display three distinct types of scattering mechanisms from the study area, represented in a grayscale image. In this image, the surface scattering values range from 0 to 0.21, which is lower than those obtained from the other two decomposition techniques, m-delta and m-chi. The double bounce scattering values range from 0 to 0.20, while the volumetric scattering values fall between 0.04 and 0.28. Notably, these values are also the lowest compared to those from the other two decomposition techniques. The lower values observed are due to the fact that the m-alpha decomposition technique is specifically designed to highlight surface scattering mechanisms. Although it is capable of differentiating between various scattering types, it tends to be less responsive to volumetric and double bounce scattering [45]. As a result, this reduced sensitivity to these more complex scattering processes leads to lower overall values in the analysis. The RGB composite of m-alpha decomposition is depicted in Figure 8b, demonstrating that, in contrast to the other two decompositions, surface scattering predominates throughout the whole region and that double bounce scattering is visible inside the crater and along its walls. The red color highlights the double bounce scattering, which occurs at the crater wall, where the surface and the wall create a natural dihedral angle.

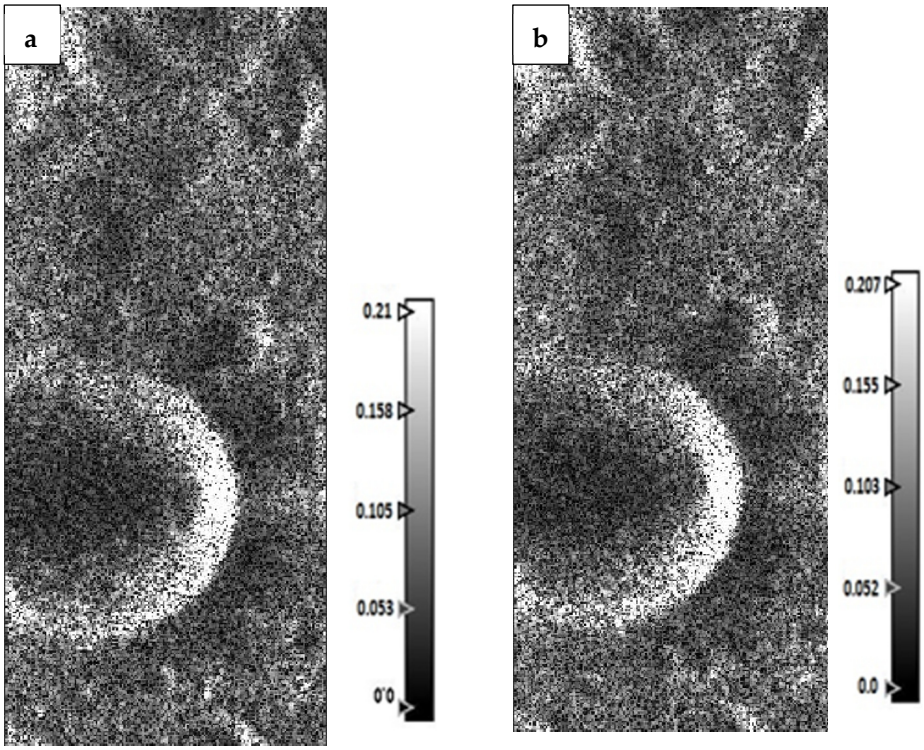

Figure 7. m-alpha (α) decomposition of Mini-SAR data Chandrayaan-1: (**a**) surface scattering; and (**b**) double bounce scattering.

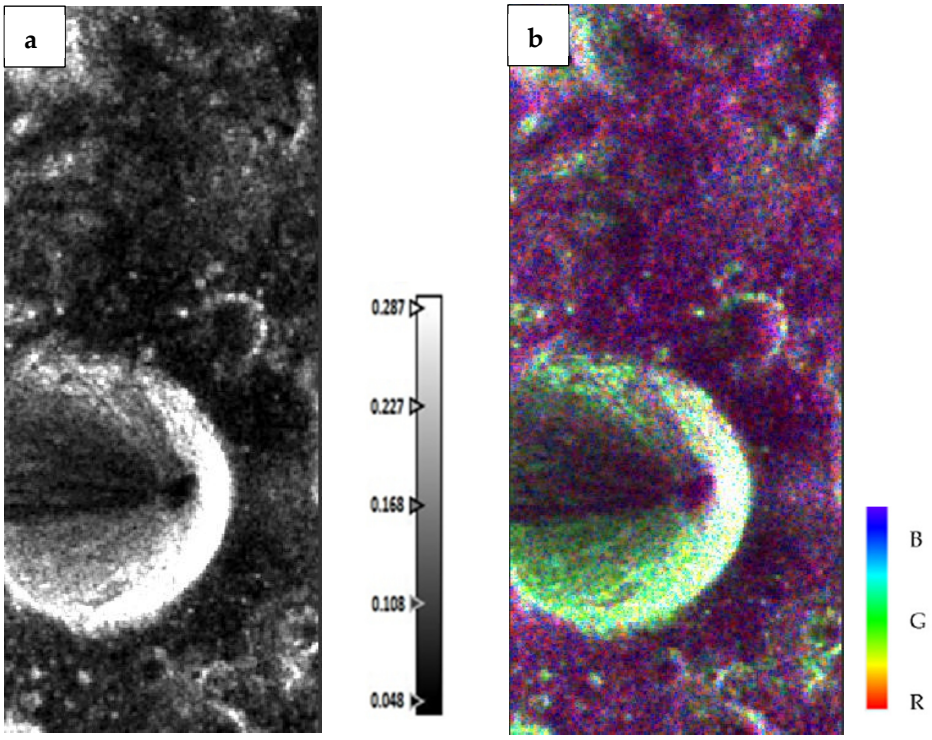

Figure 8. m-alpha decomposition of Chandrayaan-1 Mini-SAR data: (**a**) volumetric scattering; and (**b**) RGB composite where G stands for volumetric, R for double bounce, and B for surface scattering.

Comparing the image to the other two decomposition approaches, Figure 8b demonstrates that comparatively little double bounce scattering is apparent. This double bounce scattering is located near the upper section of the crater wall and along the crater rim, indicating the dihedral property of that particular area. In the lower right corner of the

crater, surface scattering is seen in blue, extending from the corner into the interior of the crater.

4.5. H-A-Alpha Decomposition

Figure 9a,b depict the Erlanger Crater's Entropy (H) and Alpha (α) images as viewed by DFSAR data, which were produced using H-A-Alpha decomposition algorithms. The Anisotropy (A) and the RGB composite of the H-A-Alpha decomposition image are displayed in Figure 10a,b, respectively. The Entropy (H), Alpha, and Anisotropy (A) are the polarization parameters that were used to derive the H-A-Alpha model. This H-A-Alpha RGB composite image helps to characterize the different types of scattering mechanisms occurring on the surface of the moon.

The Entropy (H) parameter helps determine the degree of polarization, while the mean angle alpha identifies the different scattering types present on the lunar surface. For the study area, the entropy values range from 0 to 0.99, as shown in the Figure 9a. The higher entropy values are found inside the crater and along its walls shown in blue color, which suggest the presence of both double bounce and volumetric scattering in combination.

The lower entropy values, shown in red on the right side of the crater, suggest the dominance of surface scattering in that particular area which indicates that the crater wall is smooth. These entropy results align well with the findings from other decomposition models, such as m-delta, m-chi, and m-alpha, which also show higher volumetric scattering inside the crater. The value of alpha varies from 0 to 75° as shown in Figure 9b. The parameter alpha = 45° is observed within the crater, illustrated by a transition from red to green colors, thereby suggesting the presence of volumetric scattering in that specific region. Alpha = 0° is recorded adjacent to the crater wall on the right side, as well as in the vicinity surrounding the crater, indicating surface scattering emanating from the substrate, which is represented in pink color in the accompanying Figure 9b. A minimal quantity of double bounce scattering is detected in the study region located on the upper right side of the crater, where the alpha value exceeds 45°, represented by a dark blue coloration. The value of Anisotropy (A) in most parts of the crater is between 0–0.34 as shown in Figure 10a, which indicates the scattering occurred from three pure targets. The RGB composite of H-A-Alpha is shown in Figure 10b, representing different scattering mechanisms where the red color inside the crater shows volumetric scattering.

4.6. Yamaguchi Four-Component Decomposition

The Figure 11 illustrates the RGB composite derived from the Yamaguchi four-component decomposition methodology from the DFSAR image. This figure displays the scattering characteristics of the crater, wherein the red color signifies double bounce scattering, the green color denotes volumetric scattering, and the blue color corresponds to surface scattering. A prominent presence of volumetric scattering is observed within the confines of the crater and crater ejecta are present outside the rim of the crater. The manifestation of volumetric scattering within the crater is also observed in alternative decomposition methodologies, including m-alpha, m-delta, and m-chi, as well as H-A-Alpha decomposition, suggesting that the interior of the crater may possess a rough surface or contain water ice encapsulated within the regolith. Certain regions of the crater exhibit surface scattering which indicates a smooth surface. The surface scattering observed on the wall of the crater marked by a red circle in Figure 11b signifies a smooth surface. The additional smaller craters located in proximity to the study area exhibit analogous findings, characterized by a predominance of volumetric scattering within the craters, along with minor regions exhibiting surface scattering. The phenomenon of double bounce scattering is not significantly observable within the confines of Carter; however, external to this area, there are minute regions exhibiting a red

hue, as denoted by the yellow circle in Figure 11b, which signifies the presence of double bounce scattering. The results acquired from the Yamaguchi decomposition technique are consistent with those derived from other decomposition methodologies.

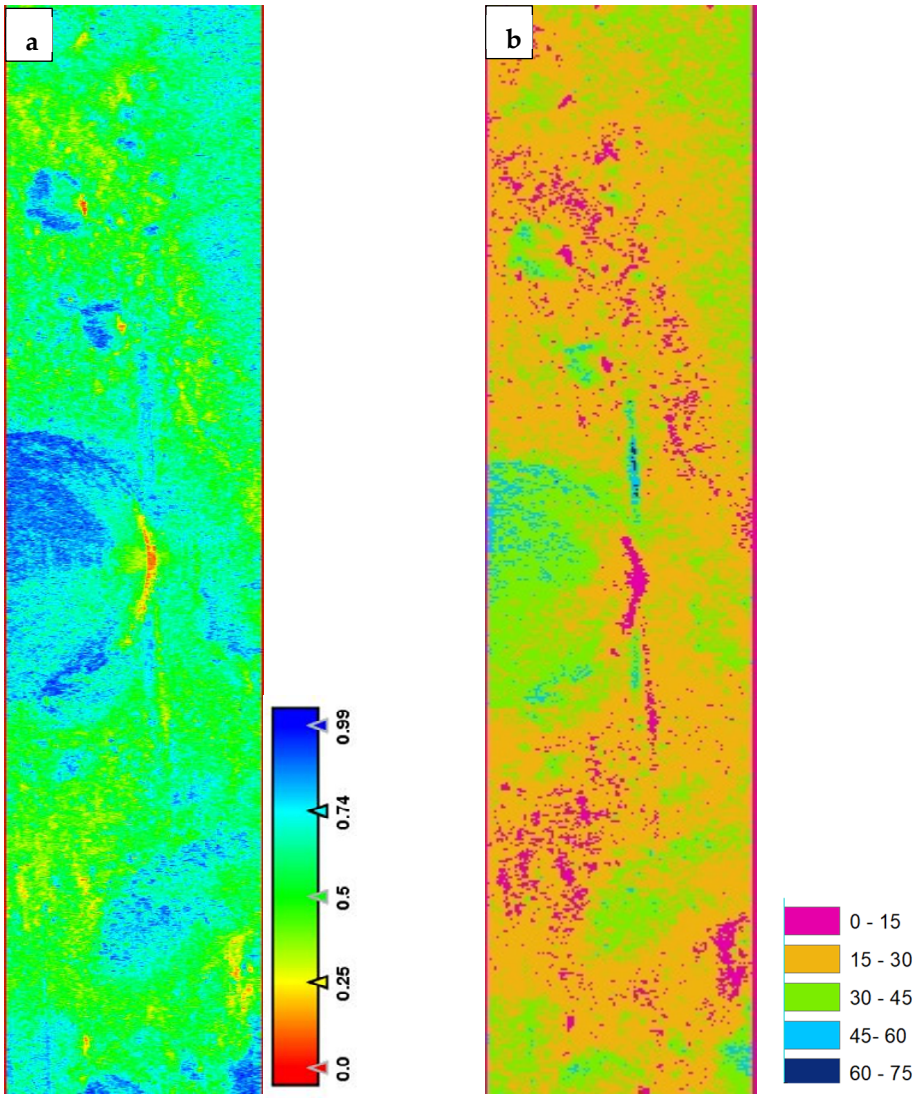

Figure 9. Eigenvalue and Eigenvector–based decomposition parameters image: (**a**) Entropy (H); and (**b**) angle alpha image.

By utilizing a range of decomposition methodologies, such as m-δ, m-χ, m-alpha, H-A-Alpha, and Yamaguchi, this study conducts an analysis of radar backscatter to discern various scattering mechanisms. The results obtained from the previously mentioned models relevant to the study area underscore that volume scattering is a primary mechanism on the irregular surfaces of the Erlanger Crater, as illustrated by the RGB imagery across all models (Figures 4b, 6b and 8b), where the green color throughout the crater's interior and its adjacent zones near edges signifies that volumetric scattering predominates across a substantial portion of the region, thereby indicating the existence of subsurface heterogeneities or ice deposits, and, consequently, implying the possible existence of underlying structures that may harbor ice. Conversely, the presence of a blue coloration, particularly near the bottom of the crater, indicates surface scattering, which may be associated with the smooth texture observed at the crater's bottom. The results suggest that an increase in surface roughness markedly enhances volume scattering, thereby reinforcing the hypothesis regarding the presence of ice. This volumetric scattering holds significant importance,

as it yields insights into subsurface characteristics, particularly within lunar craters where materials such as a regolith and potential ice deposits are present. Building upon previous research, exemplified by [44], the research work noted that elevated circular polarization ratios (CPRs) in conjunction with substantial volume scattering serve as indicators of ice deposits. Ref. [46] reported the critical role of polarimetric radar data in the identification of potential water ice deposits through the analysis of volume scattering behaviors associated with diverse surface materials. Additionally, ref. [22] offers empirical evidence demonstrating that increased crater roughness intensifies volume scattering, thereby suggesting a strong correlation between the physical properties of the surface and the existence of subsurface ice. This region is also juxtaposed with the findings of [44], which reveal somewhat analogous results. The research indicates that the surface roughness of the crater, particularly at its peripheries and base, as illustrated in Figures 4b, 6b and 8b, can significantly affect the observed magnitude of volume scattering. More rough surfaces facilitate multiple internal reflections within the material, thereby enhancing volume scattering and providing further corroboration for the potential presence of water ice in these locales. From the aforementioned conclusions and the referenced literature [22,44,46], the surface and edges of the Erlanger Crater were analyzed, thereby substantiating the findings related to water ice.

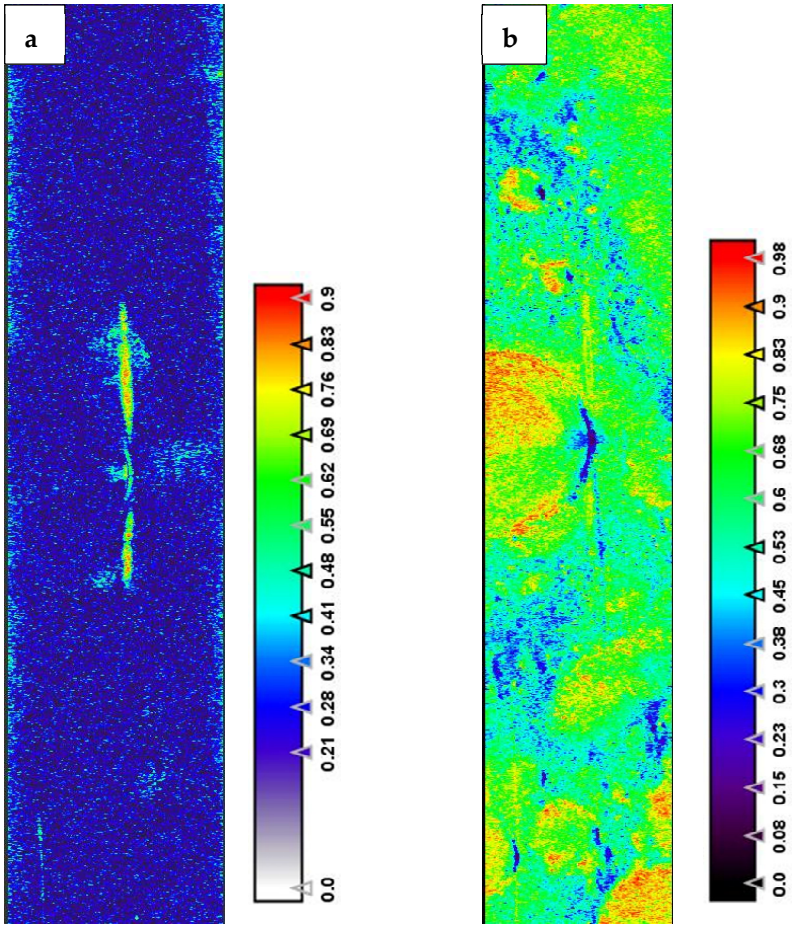

Figure 10. Eigenvalue- and Eigenvector-based parameter: (**a**) Anisotropy (A) and (**b**) RGB image of H-A-Alpha(α) decomposition modelling.

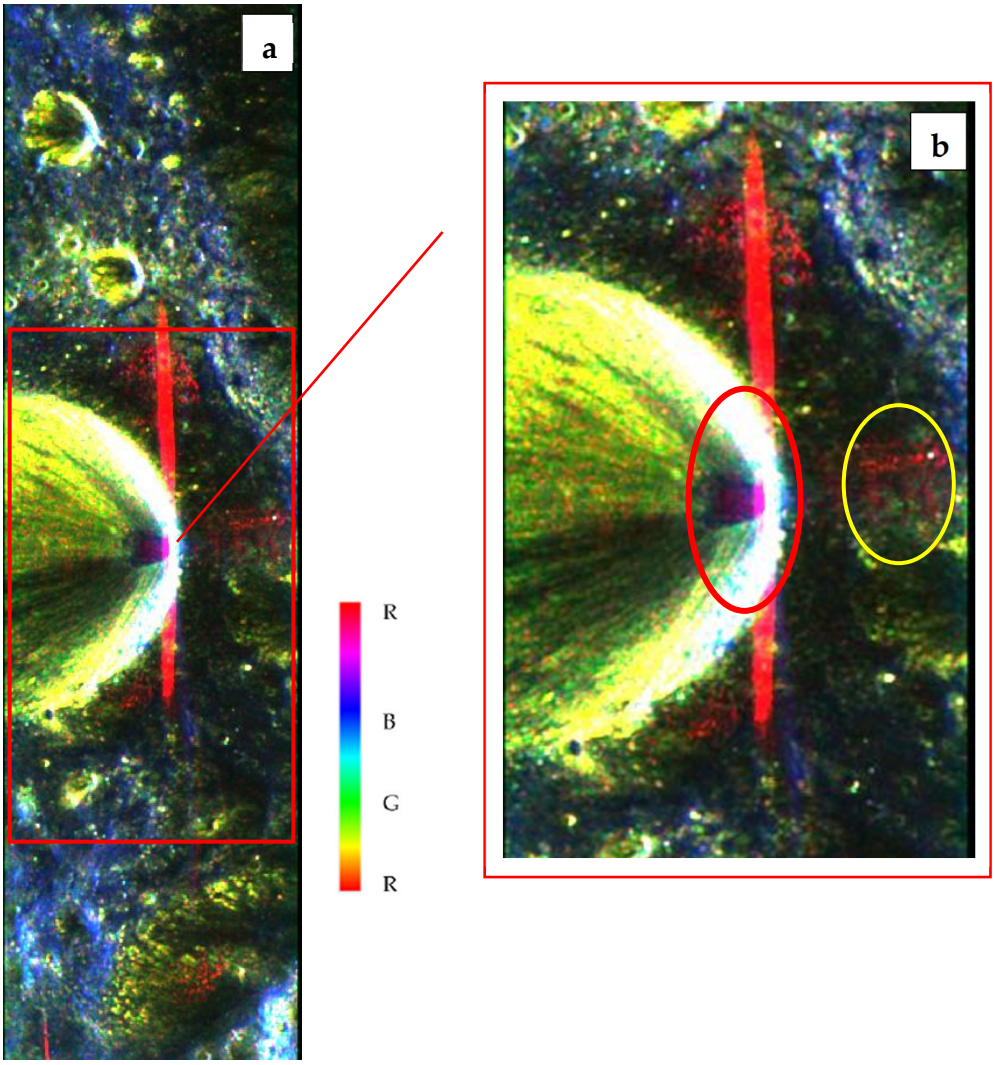

Figure 11. Yamaguchi four-component decomposition for DFSAR data: (**a**) full view of the study area, Erlanger Crater; and (**b**) closed view of the study area showing three types of scattering, namely, surface, double bounce, and volumetric.

4.7. CPR Analysis for Water Ice Deposits

The Figure 12a,b represents the image of the circular polarization ratio (CPR) derived from Mini-SAR data alongside the CPR derived from DFSAR data. The CPR serves as a fundamental metric and a significant indicator of both a rough surface and the presence of water ice deposits. A CPR value below 0.4 signifies a relatively smooth surface, whereas a higher CPR value suggests a decahedral or rough surface texture. Furthermore, a CPR value exceeding 1 denotes the existence of water ice within the regolith.

Figure 12a,b represents the CPR values derived from the Mini-SAR aboard Chandrayaan-1 and the DFSAR aboard Chandrayaan-2. The high CPR values exceeding 1, as denoted by the red color, are localized within the crater and in the vicinity of the crater's rim. Such heightened CPR values surpassing 1 signify the potential presence of water ice within that region. Furthermore, these increased CPR values may also be attributable to the roughness of the surface. Conversely, CPR values falling below the unity are represented by the yellow to green coloration in Figure 12a,b, suggesting surface scattering phenomena. To substantiate the findings of the CPR analysis, we have undertaken a comparative examination of our results against those documented in extant literature. For instance, ref. [26] conducted a thorough investigation into the characterization of the Erlanger Crater utilizing bistatic angle calculations and CPR assessments derived from

Mini-SAR data, wherein they reported a CPR value exceeding 1. Additionally, another study by [44] employed DFSAR data for the characterization of the Erlanger Crater and executed CPR analyses pertaining to the presence of water ice, revealing a CPR value range from 0 to 5.14. The results derived from these earlier published studies demonstrate a significant level of alignment with our CPR analysis, thus offering corroborative evidence for our research pursuits.

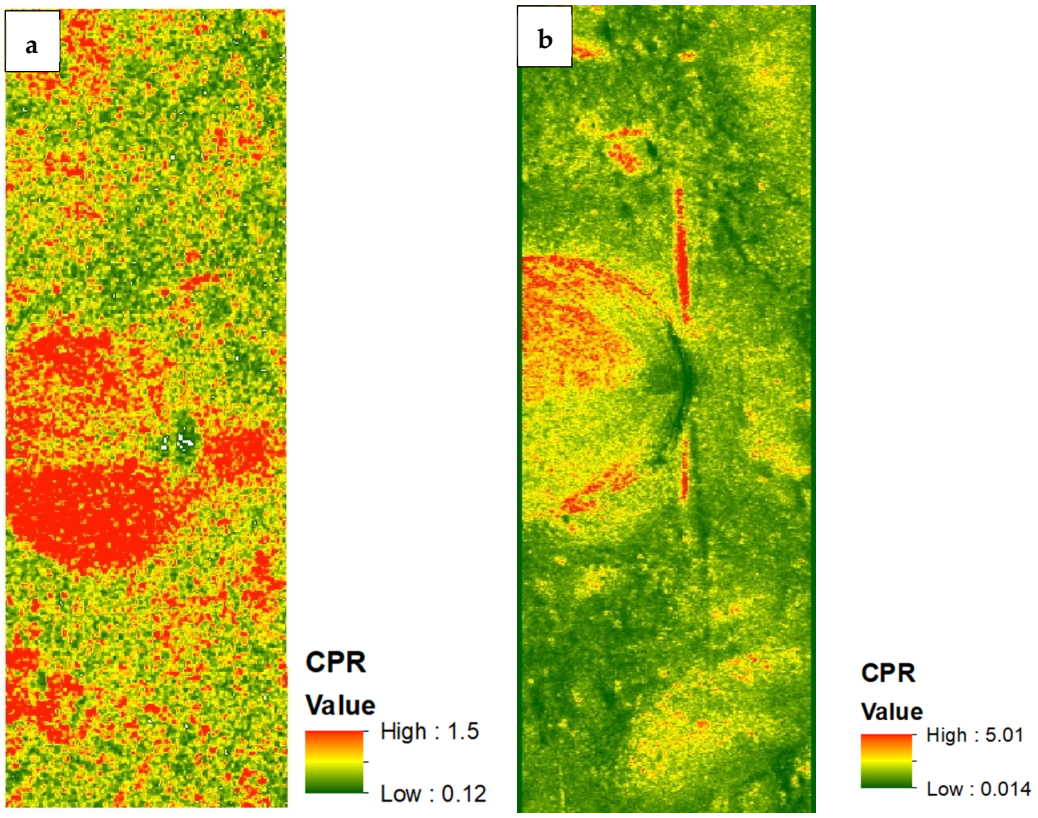

Figure 12. CPR value of Erlanger Crater: (**a**) Mini-SAR data—Chandrayaan-1; and (**b**) DFSAR data—Chandrayaan-2.

Here, in this study, the value of CPR for DFSAR data is higher than the Mini-SAR data. The elevated variation in CPR values for both datasets can be attributed to the disparities in their operational wavelength bands. The DFSAR dataset, characterized by its L band frequency, possesses a greater capacity for subsurface penetration compared to the Mini-SAR dataset, which operates within the S band. Such differences may result in interactions with increased surface roughness and an augmented same-sense polarization return, thereby contributing to the elevated CPR values observed. In the analysis of CPR derived from Mini-SAR data, the maximum recorded value of CPR is 1.5, which is predominantly associated with the lower region of the crater wall and along the right side of the crater. Conversely, the CPR value extracted from DFSAR data reveals a higher value of 5.01 in the upper section of the crater, situated within the wall, alongside several smaller areas exhibiting elevated CPR in the lower wall of the crater. Additionally, the right wall of the crater demonstrates an increased CPR value, which aligns cohesively with the CPR values obtained from the Mini-SAR data. The elevated CPR value observed in the vicinity of the crater wall may be attributed to the dihedral characteristics of the surface, which instigate the double bounce scattering phenomena of electromagnetic waves. When evaluating the various decomposition methodologies, including m-delta, m-chi, m-alpha, H-A-Alpha, and Yamaguchi decomposition, it is observed that a greater CPR value is

evident in regions characterized by volumetric scattering, specifically within the inside of the crater area.

The angle of incidence represents a pivotal element in the examination of the circular polarization ratio (CPR) values obtained from Mini-SAR and DFSAR datasets, as it considerably influences the scattering mechanisms inherent in the interaction of radar signals with both the lunar surface and its subsurface. The Mini-SAR dataset employed in this investigation operates at a consistent incidence angle of approximately 35°. At this specified incidence angle, radar waves predominantly engage with the lunar surface, particularly on inclines or the walls of craters. Surface scattering values are notably elevated, as illustrated by CPR values that span from 0.12 to 1.5, as depicted in Figure 12a. The elevated CPR value of 1.5 predominantly signifies the double bounce scattering characteristic of the dihedral nature of the crater wall. At an incidence angle of approximately 35°, the subsurface penetration is moderate. This condition constrains the radar's capability to identify volumetric scattering and potential subsurface features, such as water ice encased within the regolith. The DFSAR data strip utilized in this study captures information at an incidence angle of 25.99°. At the 25.99° incidence angle, radar waves interact with the surface, where they are reflected back toward the sensor indicated by lower CPR values (e.g., 0.014), which reflect areas with minimal scattering, often indicative of smoother or flatter surfaces as seen in the CPR image of DFSAR (Figure 12b). In the image, areas of the crater edge and the inner regions of the crater rim will show higher CPR values (e.g., close to 5.01), indicating the presence of a volumetric scattering mechanism, which is because, at the lower incidence angle (around 25.99°), radar penetrates deeper into the surface, enabling it to interact with subsurface features and materials.

5. Conclusions

The primary aim of this research endeavor is to identify the existence and possibility of water ice deposits within the Erlanger Crater located at the lunar north pole, employing the Mini Synthetic Aperture Radar data from Chandrayaan-1 alongside the DFSAR data from Chandrayaan-2. To facilitate the detection of water ice, a comprehensive physical characterization of the lunar surface was performed through the application of various decomposition methodologies, including m-δ, m-χ, m-α, H-A-Alpha, and the Yamaguchi four-component decomposition model. By implementing these diverse decomposition techniques, three distinct scattering mechanisms—namely, surface scattering, volumetric scattering, and double bounce scattering—were analyzed for the lunar surface, thereby contributing to the understanding of the dispersion of water ice in the Erlanger Crater and its surroundings. The crater showed the dominance of volumetric scattering inside the walls and the same results were obtained from all the decomposition techniques. To substantiate the findings, the circular polarization ratio (CPR) was computed for both the hybrid polarimetry Mini-SAR dataset and the fully polarimetric DFSAR dataset. A CPR value exceeding 1 was determined, indicating a significant presence of volumetric scattering within the study region, thereby implying a potential occurrence of water ice within the crater. Furthermore, this investigation was juxtaposed with the findings presented by [44], which posited that elevated CPR values coupled with the presence of volumetric scattering serve as indicators of water ice existence. Since the capability of CPR alone is insufficient to ascertain the existence of water ice on the lunar surface, it is imperative to compute additional parameters for the investigation. This research work seeks to ascertain the potential for water ice by examining the physical attributes of the lunar surface through various decomposition models and CPR values, as informed by an extensive review of relevant literature and previous studies. To enhance future research in this area, we recommend incorporating independent validation methods, such as optical datasets like

the Moon Mineralogy Mapper from Chandrayaan 1 and the Imaging Infrared Spectrometer from Chandrayaan 2, to improve the accuracy of water ice detection. Furthermore, the application of advanced machine-learning techniques to estimate the dielectric constant of the lunar surface could enhance detection by identifying complex data patterns. Expanding this methodology to additional lunar regions, such as other craters or polar areas, could contribute significantly to a broader understanding of water ice distribution on the Moon. These future directions will help build upon the foundation established by this research and support further exploration of lunar resources.

Author Contributions: Conceptualization, C.S. and S.K.; methodology, C.S.; software, C.S. and S.K.; validation, S.K., H.G. and S.L.C.; formal analysis, S.K., H.G. and S.L.C.; investigation.; S.K., H.G. and S.L.C.; resources, S.K., H.G. and S.L.C.; data curation, S.K.; writing—C.S.; writing—review and editing.; S.K., H.G. and S.L.C.; visualization, S.K., H.G. and S.L.C.; supervision, S.K., H.G. and S.L.C.; project administration, H.G.; funding acquisition, H.G. All authors have read and agreed to the published version of the manuscript.

Funding: This research did not receive any specific grant from funding agencies in the public, commercial, or not-for-profit sectors.

Data Availability Statement: The Mini SAR data is available through the Planetary Data System (PDS) Geosciences Node at [https://pds-geosciences.wustl.edu/dataserv/moon.html] (accessed on 10 March 2015), while the DFSAR data can be accessed via the PRADAN portal at [https://pradan.issdc.gov.in], (accessed on 10 March 2015).

Acknowledgments: The authors would like to express their sincere gratitude to ISRO for providing the Chandrayaan 1 Mini-SAR and Chandrayaan 2 DFSAR dataset.

Conflicts of Interest: The authors declare no conflict of interest.

References

1. Moon Facts—NASA Science. Available online: https://science.nasa.gov/moon/facts/ (accessed on 21 November 2024).
2. Singh, A.; Sharma, A.; Kumar, S.; Chang, L.; Vashishtha, A.; Raj, R.; Agrawal, S.; Chauhan, P. Dielectric characterization and polarimetric analysis of lunar north polar crater Hermite-A using Chandrayaan-1 Mini-SAR, Lunar Reconnaissance Orbiter (LRO) Mini-RF, and Chandrayaan-2 DFSAR data. *Adv. Space Res.* **2022**, *70*, 4030–4055. [CrossRef]
3. Chauhan, P.; Kaur, P.; Srivastava, N.; Sinha, R.K. Hyperspectral Remote Sensing of Planetary Surfaces: An Insight Into Composition of Inner Planets and Small Bodies in the Solar System. 2015. Available online: https://www.researchgate.net/publication/282237521 (accessed on 10 March 2015).
4. Sharma, A.; Kumar, S.; Bhiravarasu, S.S. Synergistic use of remote sensing data and in-situ investigations to characterize the lunar surface. *Adv. Space Res.* **2024**, *73*, 2155–2174. [CrossRef]
5. Kumar, S.; Kumar, A. Preface: Synergistic use of remote sensing data and in-situ investigations to reveal the hidden secrets of the moon. *Adv. Space Res.* **2024**, *73*, 2135–2136. [CrossRef]
6. Kumari, H.; Bhardwaj, A. Analysis of Polarimetric Mini-SAR and Mini-RF Datasets for Surface Characterization and Crater Delineation on Moon. *Environ. Sci. Proc.* **2021**, *4*, 10. [CrossRef]
7. Stern, S.A. The lunar atmosphere: History, status, current problems, and context. *Rev. Geophys.* **1999**, *37*, 453–491. [CrossRef]
8. Hodges, R.R.; Hoffman, J.H.; Johnson, F.S. The lunar atmosphere. *Icarus* **1974**, *21*, 415–426. [CrossRef]
9. Shukla, S.; Kumar, S.; Tolpekin, V.A. Petrophysical Insights Into Lunar Mafic Extrusive Basalts Over Reiner Gamma Formation. *IEEE J. Sel. Top. Appl. Earth Obs. Remote Sens.* **2019**, 1–17. [CrossRef]
10. Vashishtha, A.; Kumar, S. Characterization of geomorphological features of lunar surface using Chandrayaan-1 Mini-SAR and LRO Mini-RF data. *Quat. Int.* **2021**, *575–576*, 338–357. [CrossRef]
11. Shukla, S.; Kumar, S.; Tolpekin, V.A. Advancing to Lunar LavaTube Sensing: A New Radar Perspective of Philolaus Skylight Candidates. In Proceedings of the 50th Lunar and Planetary Science Conference 2019, The Woodlands, TX, USA, 18–22 March 2019; Lunar and Planetary Institute: Houston, TX, USA, 2019; p. 2283.
12. Vashishtha, A.; Kumar, S. Detection of New Potential Site of Lava Tube in Marius Hills Region by Three Component Decomposition Technique of LRO Mini-RF Data. In Proceedings of the 51st Lunar and Planetary Science Conference (2020), The Woodlands, TX, USA, 16–20 March 2020; p. 1880.

13. Kumar, P.A.; Kumar, S. A Spectrophotometric evaluation of lunar nearside craters Catharina and Cyrillus for estimations of FeO, optical maturity and TiO_2. *Adv. Space Res.* **2024**, *73*, 2203–2231. [CrossRef]
14. Shukla, S.; Kumar, S.; Agrawal, S. Mineral mapping of FeO and TiO_2 of the Cassini crater using Moon Mineralogy Mapper (M3) of Chandrayaan-1. In Proceedings of the 38th Asian Conference on Remote Sensing—Space Applications: Touching Human Lives, ACRS 2017, New Delhi, India, 23–27 October 2017; Asian Association on Remote Sensing (AARS): New Delhi, India, 2017.
15. Klaver, M.; Klemme, S.; Liu, X.-N.; Hin, R.C.; Coath, C.D.; Anand, M.; Lissenberg, C.J.; Berndt, J.; Elliott, T. Titanium-rich basaltic melts on the Moon modulated by reactive flow processes. *Nat. Geosci.* **2024**, *17*, 118–123. [CrossRef]
16. Kumar, P.A.; Kumar, S. Estimation of optical maturity parameter for lunar soil characterization using Moon Mineralogy Mapper (M3). *Adv. Space Res.* **2014**, *53*, 1694–1719. [CrossRef]
17. Sharma, A.; Kumar, S.; Bhiravarasu, S.S. Integral equation modeling for dielectric retrieval of the lunar surface using Chandrayaan-2 fully-Polarimetric L-band dual frequency SAR (DFSAR) data. *Icarus* **2023**, *391*, 115350. [CrossRef]
18. Shukla, S.; Tolpekin, V.; Kumar, S.; Stein, A. Investigating the Retention of Solar Wind Implanted Helium-3 on the Moon from the Analysis of Multi-Wavelength Remote Sensing Data. *Remote Sens.* **2020**, *12*, 3350. [CrossRef]
19. Shukla, S.; Patterson, G.W.; Maiti, A.; Kumar, S.; Dutton, N. Inferring the Variability of Dielectric Constant on the Moon from Mini-RF S-Band Observations. *Remote Sens.* **2024**, *16*, 3208. [CrossRef]
20. Woodhouse, I.H. *Introduction to Microwave Remote Sensing*; CRC Press: Boca Raton, FL, USA, 2017.
21. Dsouza, H.; Kumar, S. Characterization of the Moon's South polar craters using optical, microwave and thermal remote sensing. *Adv. Space Res.* **2024**, *73*, 2297–2322. [CrossRef]
22. Deutsch, A.N.; Head, J.W.; Neumann, G.A.; Kreslavsky, M.A.; Barker, M.K. Assessing the Roughness Properties of Circumpolar Lunar Craters: Implications for the Timing of Water-Ice Delivery to the Moon. *Geophys. Res. Lett.* **2020**, *47*, e2020GL087782. [CrossRef]
23. Jawin, E.R.; Kiefer, W.S.; Fassett, C.I.; Bussey, D.B.J.; Cahill, J.T.S.; Dyar, M.D.; Lawrence, S.J.; Spudis, P.D. The relationship between radar scattering and surface roughness of lunar volcanic features. *J. Geophys. Res. Planets* **2014**, *119*, 2331–2348. [CrossRef]
24. Kumar, S.; Singh, A.; Sharma, A.; Chaudhary, V.; Joshi, A.; Agrawal, S.; Chauhan, P. Polarimetric analysis of L-band DFSAR data of Chandrayaan-2 mission for ice detection in permanently shadowed regions (PSRs) of lunar South polar craters. *Adv. Space Res.* **2022**, *70*, 4000–4029. [CrossRef]
25. Spudis, P.D.; Bussey, D.B.J.; Baloga, S.M.; Cahill, J.T.S.; Glaze, L.S.; Patterson, G.W.; Raney, R.K.; Thompson, T.W.; Thomson, B.J.; Ustinov, E.A. Evidence for water ice on the Moon: Results for anomalous polar craters from the LRO Mini-RF imaging radar. *J. Geophys. Res. Planets* **2013**, *118*, 2016–2029. [CrossRef]
26. Verma, N.; Mishra, P.; Purohit, N.; Jain, S. Applications of Bistatic Mini-RF SAR Data for Characterization of the Erlanger Crater. *J. Indian Soc. Remote Sens.* **2022**, *51*, 165–175. [CrossRef]
27. Li, S.; Lucey, P.G.; Milliken, R.E.; Hayne, P.O.; Fisher, E.; Williams, J.-P.; Hurley, D.M.; Elphic, R.C. Direct evidence of surface exposed water ice in the lunar polar regions. *Proc. Natl. Acad. Sci. USA* **2018**, *115*, 8907–8912. [CrossRef]
28. Crater Erlanger: Where the Sun Don't Shine on the Moon. Available online: https://www.outerspaceuniverse.org/crater-erlanger-shadow-moon.html (accessed on 21 November 2024).
29. Bhandari, N.; Srivastava, N. Active moon: Evidences from Chandrayaan-1 and the proposed Indian missions. *Geosci. Lett.* **2014**, *1*, 11. [CrossRef]
30. Patterson, G.W.; Bhiravarasu, S.S.; Carter, L.M.; Cahill, J.T.S.; Chakraborty, T.; Das, A.K.; Heggy, E.; Kumar, R.; Morgan, G.A.; Neish, C.D.; et al. Characterizing the Scattering Properties of the Moon with the LRO Mini-RF and Chandrayaan-2 DFSAR Radars. In Proceedings of the 51st Annual Lunar and Planetary Science Conference, The Woodlands, TX, USA, 16–20 March 2020; p. 2507.
31. Kausika, B.B. Polarimetric Modeling of Lunar Surface for Scattering Information Retrieval Using Mini-SAR Data of Chandrayaan-1. Master's Thesis, Faculty of Geo-information Science and Earth Observation, University of Twente, Enschede, The Netherlands, 2013.
32. Raney, R.; Spudis, P.D.; Bussey, B.; Crusan, J.; Jensen, J.R.; Marinelli, W.; McKerracher, P.; Neish, C.; Palsetia, M.; Schulze, R.; et al. The Lunar Mini-RF Radars: Hybrid Polarimetric Architecture and Initial Results. *Proc. IEEE* **2011**, *99*, 808–823. [CrossRef]
33. Cloude, S.; Zebker, H. Polarisation: Applications in Remote Sensing. *Phys. Today* **2010**, *63*, 53–54. [CrossRef]
34. Singh, A. Polarimetric Modeling of Dual Frequency SAR Data for Characterization of the Lunar Surface. Master's Thesis, University of Twente, Enschede, The Netherlands, November 2021. Available online: http://essay.utwente.nl/89538/ (accessed on 20 January 2021).
35. Vyas, A.; Nizalapur, V.; Chhasia, P.; Rawal, D.; Jain, G.; Das, A. Analysis Of Different Polarimetric Decomposition Techniques Using Compact Polarimetric Nisar Data for Ahmedabad, India. *Int. Arch. Photogramm. Remote Sens. Spat. Inf. Sci.* **2021**, *XLIII-B3-2021*, 135–140. [CrossRef]
36. Cloude, S.R.; Pottier, E. An entropy based classification scheme for land applications of polarimetric SAR. *IEEE Trans. Geosci. Remote Sens.* **1997**, *35*, 68–78. [CrossRef]

37. Tomar, K.; Singh, S.; Tolpekin, V. Hybrid polarimetric decomposition for aboveground biomass estimation using semi-empirical modelling. In Proceedings of the NISAR Science & Applications Workshop, Ahmedabad, India, 19–20 November 2015.
38. Cloude, S.R.; Goodenough, D.G.; Chen, H. Compact Decomposition Theory. *IEEE Geosci. Remote Sens. Lett.* **2012**, *9*, 28–32. Available online: https://api.semanticscholar.org/CorpusID:10729902 (accessed on 11 July 2011). [CrossRef]
39. Jayasri, P.V.; Sundari, H.S.V.U.; Kumari, E.V.S.S.; Prasad, A.V.V. M-delta Decomposition of Hybrid Dual-Polarimetric RISAT-1 SAR Data. 2013. Available online: https://api.semanticscholar.org/CorpusID:14820021 (accessed on 14 December 2013).
40. Raney, R.K. Dual-polarized SAR and stokes parameters. *IEEE Geosci. Remote Sens. Lett.* **2006**, *3*, 317–319. [CrossRef]
41. Fa, W.; Cai, Y. Circular polarization ratio characteristics of impact craters from Mini-RF observations and implications for ice detection at the polar regions of the Moon. *J. Geophys. Res. Planets* **2013**, *118*, 1582–1608. [CrossRef]
42. Thompson, T.W.; Ustinov, E.A.; Heggy, E. Modeling radar scattering from icy lunar regoliths at 13 cm and 4 cm wavelengths. *J. Geophys. Res. Planets* **2011**, *116*, E01006. [CrossRef]
43. Yang, R.; Dai, B.; Tan, L.; Liu, X.; Yang, Z.; Li, H. *Polarimetric Microwave Imaging*; Springer: Singapore, 2021. [CrossRef]
44. Sharma, A.; Kumar, S.; Bhiravarasu, S.S. Scattering Mechanism of Erlanger crater using Chandryaan-2 L-band DFSAR data. In Proceedings of the 53rd Lunar and Planetary Science Conference, The Woodlands, TX, USA, 7–11 March 2022.
45. Saran, S.; Das, A.; Pandey, D. Investigation of the Capability of H-α Decomposition of Compact Polarimetric SAR Data with Application to Lunar Surface. In Proceedings of the 46th Annual Lunar and Planetary Science Conference, The Woodlands, TX, USA, 16–20 March 2015; p. 1916.
46. Putrevu, D.; Chakraborty, T.; Mukhopadhyay, J.; Syed, T.H.; Bhiravarasu, S.S.; Das, A.; Pandey, D.K.; Misra, A. Lunar Impact Craters: New Perspectives from Full-Polarimetric Analysis of Chandrayaan-2 Dual-Frequency SAR Data. *J. Geophys. Res. Planets* **2023**, *128*, e2023JE007745. Available online: https://api.semanticscholar.org/CorpusID:266141215 (accessed on 8 December 2023). [CrossRef]

Disclaimer/Publisher's Note: The statements, opinions and data contained in all publications are solely those of the individual author(s) and contributor(s) and not of MDPI and/or the editor(s). MDPI and/or the editor(s) disclaim responsibility for any injury to people or property resulting from any ideas, methods, instructions or products referred to in the content.